A top-down assessment using OMI NO₂ suggests an underestimate in the NOx emissions inventory in Seoul, South Korea during KORUS-AQ

Daniel L. Goldberg[*,1,2], Pablo E. Saide[3], Lok N. Lamsal[4,5], Benjamin de Foy[6], Zifeng Lu[1,2], Jung-Hun Woo[7], Younha Kim[7], Jinseok Kim[7], Meng Gao[8], Gregory Carmichael[9], and David G. Streets[1,2]

[1]Energy Systems Division, Argonne National Laboratory, Argonne, IL 60439 USA
[2]Consortium for Advanced Science and Engineering, University of Chicago, Chicago, IL 60637, USA
[3]Department of Atmospheric and Oceanic Sciences, Institute of the Environment and Sustainability, University of California – Los Angeles, Los Angeles, CA 90095, USA
[4]Goddard Earth Sciences Technology and Research, Universities Space Research Association, Columbia, MD 21046, USA
[5]NASA Goddard Space Flight Center, Code 614, Greenbelt, MD 20771, USA
[6]Department of Earth and Atmospheric Sciences, Saint Louis University, Saint Louis, MO 63108, USA
[7]Konkuk University, 05029 Seoul, South Korea
[8]School of Engineering and Applied Sciences, Harvard University, Cambridge, MA 02138, USA
[9]Department of Chemical and Biochemical Engineering, University of Iowa, Iowa City, IA 52242, USA
Correspondence to: Daniel L. Goldberg (dgoldberg@anl.gov)

Abstract. In this work, we investigate the NO_x emissions inventory in Seoul, South Korea using a regional NASA Ozone Monitoring Instrument (OMI) NO_2 product. We first develop a regional OMI NO_2 product by re-calculating the air mass factors using a high-resolution (4×4 km²) WRF-Chem model simulation, which better captures the NO_2 shape profiles in urban regions. We then apply a model-derived spatial averaging kernel to further downscale the retrieval and account for the sub-pixel variability. These two modifications yield OMI NO_2 values in the regional product that are 1.37 larger in the Seoul metropolitan region and >2 times larger near large industrial sources. These two modifications also yield an OMI NO_2 product that is in better agreement with the Pandora NO_2 spectrometer measurements acquired during the Korea U.S.-Air Quality (KORUS-AQ) field campaign. NO_x emissions are then derived for the Seoul metropolitan area during the KORUS-AQ field campaign using a top-down approach with the standard and regional NASA OMI NO_2 products. We first apply the top-down approach to a model simulation to ensure that the method is appropriate: the WRF-Chem simulation utilizing the bottom-up emission inventory yields a NO_x emission rate of 227 ± 94 kton/yr, while the bottom-up inventory itself yields a NO_x emission rate of 198 kton/yr. Using the top-down approach on the regional OMI NO_2 product, we derive the NO_x emissions rate from Seoul to be 484 ± 201 kton/yr, and a 353 ± 146 kton/yr NO_x emissions rate using the standard NASA OMI NO_2 product. This suggests an underestimate of 53% and 36% using the regional and standard NASA OMI NO_2 products respectively. To supplement this finding, we compare the NO_2 simulated by WRF-Chem to observations of the same quantity acquired by aircraft and find a model underestimate. When NO_x emissions in the WRF-Chem model are doubled, there is better agreement with KORUS-AQ aircraft observations. Although the current work is focused on South Korea using OMI, the methodology developed in this work can be applied to other world regions using TROPOMI and future satellite datasets (e.g., GEMS and TEMPO) to produce high-quality region-specific top-down NO_x emission estimates.

1 Introduction

Nitrogen oxides ($NO_x \equiv NO + NO_2$) are a group of reactive trace gases that are toxic to human health and can transform in the atmosphere into other noxious chemical species. During ideal atmospheric conditions NO_2 can photolyze to create O_3, another toxic air pollutant with a longer atmospheric lifetime. NO_x can also transform into particulate

5   nitrate, a component of fine particulate matter ($PM_{2.5}$), another health hazard. When fully oxidized in the atmosphere, NO_x transforms into HNO_3, a key contributor to acid rain. There are some biogenic sources, but the majority of the NO_2 in our atmosphere today is emitted by anthropogenic sources (van Vuuren et al., 2011).

NO_2 is one of the easiest trace gases to observe from space because it has strong absorption features within the 400 – 465 nm wavelength region (Vandaele et al., 1998). The Dutch-Finnish Ozone Monitoring Instrument (OMI) measures

10   the absorption of solar backscatter in the UV-visible spectral range. By comparing observed spectra with a reference spectrum, the amount of NO_2 in the atmosphere between the instrument in low-earth orbit and the surface can be derived; this technique is called differential optical absorption spectroscopy (DOAS) (Platt, 1994).

Tropospheric NO_2 column contents from OMI have been used to estimate NO_x emissions from various areas around the globe (Streets et al., 2013; Miyazaki et al., 2017) including North America (Boersma et al., 2008; Lu et al., 2015),

15   Asia (Zhang et al., 2008; Han et al, 2015; Kuhlmann et al., 2015; Qu et al., 2017), the Middle East (Beirle et al., 2011), and Europe (Huijnen et al., 2010; Curier et al., 2014). It has also been used to produce and validate NO_x emission estimates from sectors such as soil (Hudman et al., 2010; Vinken et al., 2014a; Rasool et al., 2016), lightning (Allen et al., 2012; Liaskos et al., 2015; Pickering et al., 2016; Nault et al., 2017), power plants (de Foy et al., 2015), aircraft (Pujadas et al., 2011), marine vessels (Vinken et al., 2014b; Boersma et al., 2015), and urban centers (Lu et al., 2015;

20   Canty et al., 2015; Souri et al., 2016).

With a pixel resolution varying from 13×24 km^2 to 26×128 km^2, the OMI sensor was developed for global to regional scale studies rather than for individual urban areas. Even at the highest spatial resolution of 13×24 km^2, the sensor has difficulty observing the fine structure of NO_2 plumes at or near the surface (e.g., highways, power plants, factories, etc.) (Chen et al., 2009; Ma et al., 2013; Flynn et al., 2014), which are often less than 10 km in width (Heue

25   et al., 2008). This can lead to a spatial averaging of pollution (Hilboll et al., 2013). A temporary remedy, until higher spatial resolution satellite instruments are operational, is to use a regional air quality simulation to estimate the sub-pixel variability of OMI pixels. Kim et al. (2016) utilize the spatial variability in a regional air quality model to spatially downscale OMI NO_2 measurements using a spatial averaging kernel. The spatial averaging kernel technique has shown to increase the OMI NO_2 signal within urban areas, which is in better agreement with observations in these

30   regions (Goldberg et al., 2017).

Furthermore, the air mass factor and surface reflectance used in obtaining the global OMI NO_2 retrievals are at a coarse spatial resolution. While appropriate for a global operational retrieval, this is known to cause an underestimate in the OMI NO_2 signal in urban regions (Russell et al., 2011). The air mass factors in operational OMI NO_2 are calculated using NO_2 shape profiles that are provided at a $1.25° \times 1°$ spatial resolution in the NASA product (Krotkov

Atmospheric
Chemistry
and Physics
Discussions

et al. 2017) and $2° \times 3°$ spatial resolution in the DOMINO product (Boersma et al., 2011). Developers of the NASA product provide scattering weights and additional auxiliary information so that users can develop their own tropospheric vertical column product a posteriori (Lamsal et al. 2015). Several users have re-calculated the air mass factor using a regional air quality model (Russell et al., 2011; Kuhlmann et al, 2015; Lin et al., 2015; Goldberg et al.,

5   2017), which can better capture the NO_2 shape profiles in urban regions. These a posteriori products have better agreement with ground-based spectrometers measuring tropospheric vertical column contents (Goldberg et al., 2017). When available, observations from aircraft can constrain the NO_2 shape profiles used in the air mass factor calculation (Goldberg et al., 2017).

In this paper, we apply both techniques (the spatial averaging kernel and an air mass factor adjustment) to develop a

10   regional OMI NO_2 product for South Korea. We then use the regional product with only the air mass factor adjustment to derive NO_x emission estimates for the Seoul metropolitan area using an exponentially modified Gaussian (EMG) function (Beirle et al., 2011; Valin et al., 2013; de Foy et al., 2014; Lu et al., 2015); the methodology is described in-depth in Section 2.5.

2 Methods

15   **2.1 OMI NO_2**

OMI has been operational on NASA's Earth Observing System (EOS) Aura satellite since October 2004 (Levelt et al., 2006). The satellite follows a sun-synchronous, low-earth (705 km) orbit with an equator overpass time of approximately 13:45 local time. OMI measures total column amounts in a 2600 km swath divided into 60 unequal area "field-of-views", or pixels. At nadir (center of the swath), pixel size is 13×24 km^2, but at the swath edges, pixels

20   can be as large as 26×128 km^2. In a single orbit, OMI measures approximately 1650 swaths and achieves daily global coverage over $14 – 15$ orbits (99 minutes per orbit). Since June 2007, there has been a partial blockage of the detector's full field of view, which has limited the number of valid measurements by blocking consistent rows of data; this is known in the community as the row anomaly (Dobber et al., 2008): http://projects.knmi.nl/omi/research/product/rowanomaly-background.php.

25   OMI measures radiance data between the instrument's detector and the Earth's surface. Comparison of these measurements with a reference spectrum (i.e., DOAS technique), enables the calculation of the total slant column density (SCD), which represents an integrated trace gas abundance from the sun to the surface and back to the instrument's detector, passing through the atmosphere twice. For tropospheric air quality studies, vertical column density (VCD) data are more useful. This is done by subtracting the stratospheric slant column from the total

30   (tropospheric + stratospheric) slant column and dividing by the tropospheric air mass factor (AMF), which is defined as the ratio of the SCD to the VCD, as shown in Eq. (1):

$$VCD_{trop} = \frac{SCD_{total} - SCD_{strat}}{AMF_{trop}} \quad , \text{where } AMF_{trop} = \frac{SCD_{trop}}{VCD_{trop}} \qquad (1)$$

Atmospheric
Chemistry
and Physics
Discussions

The tropospheric AMF has been derived to be a function of the optical atmospheric/surface properties (viewing and solar angles, surface reflectivity, cloud radiance fraction, and cloud height) and a priori shape profile (Palmer et al., 2001; Martin et al., 2002) and can be calculated as follows (Lamsal et al., 2014) in Eq. (2):

$$AMF_{trop} = \frac{\sum_{surface}^{tropopause} SW \times x_a}{\sum_{surface}^{tropopause} x_a} \qquad (2)$$

5   where x_a is the partial column. The optical atmospheric/surface properties are characterized by the scattering weight and are calculated by a forward radiative transfer model (TOMRAD), which are output as a look-up table. The scattering weights are then adjusted real-time depending on observed viewing angles, surface albedo, cloud radiance fraction, and cloud pressure.

For this study, we follow previous studies (e.g., Palmer et al., 2001, Martin et al., 2002, Boersma et al., 2011, Bucsela
10   et al., 2013) and assume that scattering weights and trace gas profile shapes are independent. The a priori trace gas profile shapes (x_a) must be provided by a model simulation. In an operational setting, NASA uses a monthly-averaged and year-specific Global Model Initiative (GMI) global simulation with a spatial resolution of 1.25° lon × 1° lat (~110 km × 110 km in the mid-latitudes) to provide the a priori shape profiles.

We derive tropospheric VCDs using a priori NO_2 shape profiles from a regional WRF-Chem simulation. A full
15   description of this methodology can be found in Goldberg et al. (2017); it is also described in brief in section 2.1.1. We filter the Level 2 OMI NO_2 data to ensure only valid pixels are used. Daily pixels with solar zenith angles $\geq 80°$, cloud radiance fractions ≥ 0.5, or surface albedo ≥ 0.3 are removed as well as the five largest pixels at the swath edges (i.e., pixel numbers $1 - 5$ and $56 - 60$). Finally, we remove any pixel flagged by NASA including pixels with NaN values, 'XTrackQualityFlags' $\neq 0$ or 255 (RA flag), or 'VcdQualityFlags' > 0 and least significant bit $\neq 0$ (ground
20   pixel flag).

2.1.1 OMI-WRF-Chem NO_2

We modify the air mass factor in the OMI NO_2 retrieval based on the vertical profiles from a high spatial (4×4 km^2) resolution WRF-Chem simulation. The vertical profiles are scaled based on a comparison with in situ aircraft observations; this accounts for any consistent biases in the model simulation. To re-calculate the air mass factor for
25   each OMI pixel, we first compute sub-pixel air mass factors for each WRF-Chem model grid cell, using the same method as outlined in Goldberg et al. (2017). The sub-pixel air mass factor for each WRF-Chem grid cell is a function of the modelled NO_2 shape profile and the scattering weight calculated by a radiative transfer model. We then average all sub-pixel air mass factors within an OMI pixel (usually 10-100) to generate a single tropospheric air mass factor for each individual OMI pixel. This new air mass factor is used to convert the total slant column into a total vertical
30   column using Equation 1. Model outputs were sampled at the local time of OMI overpass. For May 2016, we used daily NO_2 profiles and terrain pressures (e.g., (Laughner et al., 2016)) to re-calculate the AMF. For other months and

years, we used May 2016 monthly mean values of NO_2 and tropopause pressures for the a priori profiles which are used in the calculation of the AMF.

Once the tropospheric vertical column of each OMI pixel was re-calculated, the product was oversampled (de Foy et al., 2009; Russell et al., 2010) for April – June over a 3-year period (2015-2017; 9 months total). During this

5   timeframe, there are approximately 9 valid OMI NO_2 pixels per month over any given location on the Korean peninsula.

2.2 NO_2 observations during KORUS-AQ

We use in situ NO_2 observations from the KORUS-AQ field campaign to test the regional satellite product. KORUS-AQ was a joint Korea-US field experiment designed to better understand the trace gas and aerosol composition above

10   the Korean peninsula using aircrafts, ground station networks, and satellites. The campaign took place between May 1, 2016 and June 15, 2016 and measurements were primarily focused in the Seoul Metropolitan Area. In this paper, we utilize data acquired by the ground-based Pandora spectrometer network and the thermally dissociated laser-induced fluorescence NO_2 instrument on DC-8 aircraft. KORUS-AQ observations were retrieved from the online data archive: http://www-air.larc.nasa.gov/cgi-bin/ArcView/korusaq. A further description of this field campaign can be

15   found in the KORUS-AQ White Paper (https://espo.nasa.gov/korus-aq/content/KORUS-AQ_Science_Overview_0)

2.2.1 Pandora NO_2 data

Measurements of total column NO_2 from the Pandora instrument (Herman et al., 2009; 2018) are used to evaluate the OMI NO_2 satellite products. The Pandora instrument is a stationary, ground-based, sun-tracking spectrometer, which measures direct sunlight in the UV-Visible spectral range (280-525 nm) with a sampling period of 90 seconds. The

20   Pandora spectrometer measures total column NO_2 using a DOAS technique similar to OMI. A distinct advantage of the Pandora instrument is that it does not require complex assumptions for converting slant columns into vertical columns, compared to zenith sky measurements (e.g., MAX-DOAS).

Valid OMI NO_2 pixels are matched spatially and temporally to Pandora total column NO_2 observations. To smooth the data and eliminate brief small-scale plumes that would be undetectable by a satellite, we average the Pandora

25   observations over a two hour period (± one hour of the overpass time) before matching to the OMI NO_2 data (Goldberg et al., 2017). During May 2016, there were seven Pandora NO_2 spectrometers operating during the experiment (five instruments were situated within the Seoul metropolitan area and their locations are shown in Figure 5); this corresponded to fifty instances in which valid Pandora NO_2 observations matched valid OMI NO_2 column data.

2.2.2 DC-8 aircraft data

30   We compare the model simulation to in situ NO_2 data gathered by the Cohen group (Thornton et al., 2000; Day et al, 2002) on the DC-8 aircraft. The instrument quantifies NO_2 via laser-induced fluorescence at 585 nm. This instrument

Atmospheric
Chemistry
and Physics
Discussions

does not have the same positive bias as chemiluminescence NO_2 detectors, so there is no need to modify NO_2 concentrations by applying an empirical equation (e.g., Lamsal et al., 2008).

We utilize one-minute averaged DC-8 data from all fourteen flights during May – June 2016. A typical flight path included several low-altitude spirals over the Seoul Metropolitan Area and a long-distance transect over the Korean peninsula or the Yellow Sea. One-minute averaged data is already pre-generated in the data archive. Hourly output from the model simulation is spatially and temporally matched to the observations. We then bin the data into different altitude ranges for our comparison.

2.3 WRF-Chem model simulation

For the high-resolution OMI NO_2 product, we use a regional simulation of the Weather Research & Forecasting (Skamarock et al., 2008) coupled to Chemistry (WRF-Chem) (Grell et al., 2005) in forecast mode prepared for flight planning during the KORUS-AQ field campaign. The forecast simulations were performed daily and used National Centers for Environmental Prediction Global Forecast System (https://rda.ucar.edu/datasets/ds084.6/) meteorological initial and boundary conditions from the 06 UTC cycle. Initial conditions for aerosols and gases were obtained from the previous forecasting cycle, while Copernicus Atmosphere Monitoring Service (Inness et al., 2015) forecasts were used as boundary conditions. WRF-Chem was configured with two domains, with 20 km and 4 km grid-spacing. The 20 km domain included the major sources for trans-boundary pollution impacting the Korean peninsula (deserts in China and Mongolia, wild-fires in Siberia and anthropogenic sources from China). The 4 km domain provided a high-resolution simulation where detailed local sources could be modeled and where the KORUS-AQ flight tracks were contained. The inner domain was started 18 hours after the outer domain, and was simulated for 33 hours (00UTC from day 1 to 9 UTC of day 2 of the forecast); output was saved hourly. The last 24 hours of each inner domain daily forecast over the course of KORUS-AQ were selected to allow spin-up from the outer domain and were used in the analysis presented here.

WRF-Chem was configured with 4 bin MOSAIC aerosols (Zaveri et al., 2008), a reduced hydrocarbon trace gas chemical mechanism (Pfister et al., 2014) including simplified secondary organic aerosol formation (Hodzic and Jimenez, 2011), and with capabilities to assimilate satellite aerosol optical depth both from low-earth orbiting and geostationary satellites (Saide et al., 2013, 2014), which to our knowledge is the first near-real time application of geostationary satellite data assimilation for air quality forecasts.

2.4 Emission Inventory

The WRF-Chem simulation was driven by emissions developed by Konkuk University. Monthly emissions for South Korea were developed using the 2015 Korean national emissions inventory, Clean Air Policy Support System (CAPSS), with enhancements by Konkuk University. The projected CAPSS 2015 emissions were estimated based on CAPSS 2012 and 3-year growth factors. Since the base year of the inventory is 2012, observed emissions from the post-2013 Large Point Source inventory were not included. Emissions from China and North Korea were taken from

the Comprehensive Regional Emissions for Atmospheric Transport Experiments (CREATE) v3.0 emissions inventory. In order to project the year 2010 emissions to 2015, the latest energy statistics from the International Energy Agency (http://www.iea.org/weo2017/) and the China Statistical Yearbook 2016 (http://www.stats.gov.cn/tjsj/ndsj/2016/indexeh.htm) were used to update the growth of fuel activities. In addition,

5   the new emissions control policies in China, which were compiled by the International Institute for Applied Systems Analysis, were applied to consider efficiencies of emissions control (van der A et al., 2017).

Emissions were first processed to the monthly time-scale at a spatial resolution of 3 km in South Korea and 0.1° for the rest of Asia using SMOKE-Asia (Woo et al., 2012). Information from GIS, such as population, road network, and land cover, were applied to generate gridded emissions from the region-based (17 metropolitan and provincial

10   boundaries of South Korea) emissions. The GIS-based population and regional boundary data compiled by the Ministry of Interior and Safety (http://www.mois.go.kr/frt/sub/a05/totStat/), and land cover data compiled by the Ministry of Environment (https://egis.me.go.kr/) were used to generate population and land cover based spatial surrogates. The Road and Railroad network data compiled by The Korea Transport Institute were used to generate spatial surrogates for onroad and nonroad emissions (https://www.koti.re.kr/). The emissions were downscaled

15   temporally from monthly to hourly and spatially re-allocated to 4 km over South Korea and 20 km over the rest of East Asia using the University of Iowa emission pre-processor (EPRES).

Biogenic emissions are included using the on-line Model of Emissions of Gases and Aerosols from Nature (MEGAN) model version 2; there are no NO_x emissions from MEGAN. For this simulation, the lightning NO_x parameterization was turned off. For wildfires we used the Quick Fire Emissions Dataset (QFED2), but there were only isolated, small

20   fires in South Korea during this timeframe.

2.5 Exponentially Modified Gaussian Fitting Method

An exponentially modified Gaussian (EMG) function is fit to a collection of NO_2 plumes observed from OMI in order to determine the NO_2 burden and lifetime from the Seoul metropolitan area. The original methodology, proposed by Beirle et al. (2011), involves the fitting of OMI NO_2 line densities to an EMG function. OMI NO_2 line densities are

25   the integral of OMI NO_2 retrieval perpendicular to the path of the plume; the units are mass per distance. We define integration length scale as the across plume width. The across plume width is dependent on the NO_2 plume size and can vary between 10 km (for small point sources) to 240 km (for large urban areas). Visual inspection of the rotated oversampled OMI NO_2 plume, is the best way to determine the spatial extent of the emission sources (Lu et al. 2015).

The EMG model is expressed as Equation (3):

30
$$OMI\ NO_2\ Line\ Density\ = \alpha \left[\frac{1}{x_o} exp \left(\frac{\mu}{x_o} + \frac{\sigma^2}{2x_o^2} - \frac{x}{x_o} \right) \Phi \left(\frac{x-\mu}{\sigma} - \frac{\sigma}{x_o} \right) \right] + \beta \qquad (3)$$

where α is the total number of NO_2 molecules observed near the hotspot, excluding the effect of background NO_2, β; x_o is the e-folding distance downwind, representing the length scale of the NO_2 decay; μ is the location of the apparent

source relative to the city center; σ is the standard deviation of the Gaussian function, representing the Gaussian smoothing length scale; Φ is the cumulative distribution function. Using the 'curvefit' function in IDL, we determine the five unknown parameters: $\alpha, x_o, \sigma, \mu, \beta$ based on the independent (distance; x) and dependent (OMI NO$_2$ line density) variables.

5   Using the mean zonal wind speed, w, of the NO$_2$ line density domain, the mean effective NO$_2$ lifetime $\tau_{effective}$ and the mean NOx emissions can be calculated from the fitted parameters x_o and α. The wind speed and direction are obtained from the ERA-Interim re-analysis project (Dee et al., 2011). We use the averaged wind fields of the bottom eight levels of the re-analysis (i.e., from the surface to ∼500 m). Only days in which the wind speeds are > 3 m/s are included in this analysis, because NO$_2$ decay under this condition is dominated by chemical removal, not variability in the winds. The factor of 1.33 is the mean column-averaged NO$_x$ / NO$_2$ ratio in the WRF-Chem model simulation

10   for the Seoul metropolitan area during the mid-afternoon.

$$NO_x \; Emissions = 1.33 \left(\frac{\alpha}{\tau_{effective}} \right), \text{ where } \tau_{effective} = \frac{x_o}{w} \qquad (4)$$

The NO$_2$ plume concentration is a function of the emission source strength, wind speed, and wind direction. Originally, the method separated all NO$_2$ plumes by wind direction, and fit an EMG function to NO$_2$ in eight wind directions

15   (Beirle et al., 2011; Ialongo et al., 2014; Liu et al., 2016). Newer methodologies rotate the plumes so that all plumes are in the same direction (Valin et al., 2013; de Foy et al., 2014; Lu et al., 2015). This process increases the signal-to-noise ratio and generates a more robust fit. In this work, we filter OMI NO$_2$ data and rotate the NO$_2$ plumes and as described in Lu et al. (2015), so that all plumes are decaying in the same direction. We rotate the retrieval based on the re-analyzed 0-500 m wind speed direction from the ERA-Interim. In doing so, we develop a re-gridded satellite

20   product in an x-y coordinate system, in which the urban plume is aligned along the x-axis. Following de Foy et al. (2014) and Lu et al. (2015), we only use days in which the wind speeds are > 3 m/s because there is more direct plume transport and less plume meandering on days with stronger winds; this yields more robust NO$_x$ emission estimates. We fit an EMG function to the line density as function of the horizontal distance. This yields a single value at each point along the x-direction.

25   **3 Results**

In this section, we describe the regional high-resolution satellite product and our validation efforts. All OMI NO$_2$ results presented here are vertical column densities. First, we show a continental snapshot of OMI NO$_2$ (OMI-Standard) over East Asia using the standard NASA product. Then, we show a regional NASA OMI NO$_2$ satellite product (OMI-Regional) using AMFs generated from the WRF-Chem a priori NO$_2$ profiles. We compare the OMI-

30   Regional product with NO$_2$ VCDs from the original WRF-Chem simulation. We evaluate the OMI-Regional product by comparing to KORUS-AQ observations. Finally, we use the OMI-Standard and OMI-Regional products to estimate NO$_x$ emissions from the Seoul metropolitan area.

3.1 OMI NO$_2$ in East Asia

Oversampled OMI NO$_2$ for May – September 2015 – 2017 (15 months total) in East Asia and the US is shown in Figure 1. The OMI NO$_2$ signals in East Asia over major metropolitan areas are 3 to 5 times larger than over similarly sized cities in the US. This is in despite of recent NO$_x$ reductions in China since 2011 (de Foy et al., 2016b; Souri et

5   al., 2017). OMI has observed a recent decrease in the NO$_2$ burden in the immediate Seoul, South Korea metropolitan area, but an increase in areas just outside the city center (Duncan et al., 2016). Oversampled values greater than 8×10^{15} molecules per cm^2 are still consistently seen in East Asia, while they are non-existent in the US.

3.2 Calculation of new OMI tropospheric column NO$_2$

In Figure 2, we plot the OMI-Standard and OMI-Regional products over South Korea. The top panels show a regional

10   product in which only the air mass factor correction is applied (AMF). The bottom panels show a regional product in which the air mass factor correction and spatial averaging kernel are applied (AMF+SK). The regional product yields larger OMI NO$_2$ values throughout the majority of the Korean peninsula. Areas near major cities (e.g. Seoul), power plants, steel mills, and cement kilns have OMI NO$_2$ values that are >1.25 times larger in the regional AMF product and >2 times larger in the regional AMF+SK product. There are two reasons for the larger OMI NO$_2$ signals: the air

15   mass factors in polluted regions are now smaller (Russell et al., 2011; Goldberg et al., 2017) and the spatial weighting kernel allocates a large portion of the OMI NO$_2$ signal into a smaller region (Kim et al., 2016). There are small decreases in the northeastern Korean peninsula due to an increase in the air mass factors in these regions.

3.3 OMI-Regional vs. WRF-Chem

We now compare the OMI-Regional product to tropospheric vertical columns from the WRF-Chem model simulation

20   directly. In Figure 3, we compare the regional satellite product to the WRF-Chem simulation over the Korean peninsula. In all areas, the modeled tropospheric column NO$_2$ is of smaller magnitude than inferred by the satellite. In the area within 40 km of the Seoul city center, modeled tropospheric vertical columns are 44% smaller than observed tropospheric vertical column in the regional AMF+SK product. We posit three reasons as to why the model simulation calculates columns that are consistently smaller. First, WRF-Chem uses a reduced hydrocarbon gas-phase chemical

25   mechanism. This fast-calculating mechanism implemented in WRF-Chem for regional climate assessments (Pfister et al., 2014) and used during KORUS-AQ for forecasting does not quickly recycle alkyl nitrates back to NO$_2$; this will cause NO$_2$ to be too low. While an underestimate of the chemical conversion to NO$_2$ in WRF-Chem is a contributor to the underestimate, it likely does not account for the entire discrepancy; Canty et al., (2015) suggests that by shortening the lifetime of alkyl nitrates in the chemical mechanism, NO$_2$ will increase by roughly 3% in urban areas

30   and 18% in rural areas. Second, the temporal allocation of NO$_x$ emissions in this WRF-Chem simulation is such that the early afternoon rate (between 12:00 – 14:00 local time) is approximately equal to 24-hour averaged rate. For comparison, using SMOKE in the eastern US yields an early afternoon emission rate that is 1.35 larger than the 24-hour averaged emission rate. Lastly, the remaining difference will likely be due to an underestimate in the emissions inventory.

3.3.1 Comparing WRF-Chem to Aircraft Measurements

When comparing the model simulation to in situ observations from the UC-Berkeley NO_2 instrument aboard the aircraft, we find that NO_2 concentrations are substantially larger than the model when spatially and temporally co-located in the immediate Seoul metropolitan area (Figure 5). The comparison isolates the NO_2 within the lowermost

5   boundary layer as the primary contributor to the tropospheric column underestimate. When comparing aircraft NO_2 to modeled NO_2 in other areas of the Korean peninsula, the underestimate is consistently smaller. This suggests a larger underestimate in the NO_x emissions inventory in the immediate Seoul metropolitan area.

3.4 Comparison of OMI NO_2 to Pandora NO_2

To quantify the skill of the regional OMI NO_2 product, we compare the new total NO_2 vertical columns from the

10   satellite product to the same quantities observed by the Pandora instruments. In Figure 6, monthly averaged observations during May 2016 from the Pandora instrument are overlaid onto the monthly average of the three OMI NO_2 satellite products. The two regional OMI NO_2 products capture the magnitude and spatial variability of monthly averaged NO_2 within the metropolitan region better.

We then compare daily Pandora observations to each daily OMI NO_2 value spatially and temporally co-located with

15   the Pandora instrument. The Pandora observation is a 2-hour mean centered on the mid-afternoon OMI overpass. The slope of the linear best-fit of the standard product is 0.58, indicating that there is a consistent low bias in the satellite product when the Pandora instrument observes large values. The best-fit slope of the OMI-Regional product with only the air mass factor adjustment (AMF) is 0.76 and the OMI-Regional product with the air mass factor adjustment and spatial kernel (AMF+SK) is 1.07, indicating that the regional products capture the polluted-to-clean

20   spatial gradients best. The correlation of daily observations to the satellite retrievals does not improve between retrievals.

3.5 Estimating NO_x emissions from Seoul

To estimate NO_x emissions from the Seoul metropolitan area using a top-down satellite-based approach, we follow the exponentially modified Gaussian (EMG) fitting methodology outlined in Section 2.5. When fit using the EMG

25   method, the photochemical lifetime and OMI NO_2 burden can be derived. Using this information, a NO_x emission rate can be inferred.

3.5.1. Validating the EMG method using WRF-Chem

The WRF-Chem simulation can serve as a test bed to assess the accuracy of the EMG method, since the bottom-up emissions used for the simulation are known. For this study, we find that for Seoul, an across plume width of 160 km

30   encompasses the entire NO_2 downwind plume. Using the NO_2 lifetime, NO_2 burden, and a 160 km across plume width, we calculate the top-down NO_x emissions rate in the WRF-Chem simulation from the Seoul metropolitan area during the early afternoon (Figure 7). We find the effective NO_2 photochemical lifetime to be 3.1 ± 1.3 hours and the

emissions rate to be 227 ± 94 kton/yr NO_2 equivalent. Uncertainties of the top-down NO_x emissions are the square root of the sum of the squares of: the NO_x / NO_2 ratio (10%), the OMI NO_2 vertical columns (25%), the across plume width (10%), and the wind fields (30%). Only the latter three terms are used to calculate the uncertainty of the NO_2 lifetime.

5   The NO_x bottom-up emissions inventory calculated using a 40 km radius from the Seoul city center is 198 kton/yr NO_2 equivalent. We use a 40 km radius in lieu of a larger radius because an assumption in EMG method is that the emissions must be clustered around a single point (in this case, the city center). Therefore, the calculated emissions rate from the EMG fit is only measuring the magnitude of the perturbing emission source, and not of smaller sources that are further from the city center. Previous studies (de Foy et al., 2014; de Foy et al., 2015) suggest that the
10   background level calculated by the EMG fit accounts for emissions outside the plume that are more regional and diffuse in nature. The agreement between the top-down (227 kton/yr) and bottom-up (198 kton/yr) approaches demonstrates the accuracy and effectiveness of the EMG method in estimating the emissions rate.

3.5.2. Deriving emissions using OMI NO_2

We now calculate the top-down NO_x emissions rate from the satellite data from the Seoul metropolitan area during
15   the early afternoon (Figure 8). Here we use the OMI standard product and the OMI NO_2 retrieval without the spatial averaging kernel; only the new air mass factor is applied to this retrieval. We do not use the retrieval with the spatial averaging kernel when calculating top-down NO_x emissions because the spatial averaging is strongly dependent on the wind fields in the WRF-Chem simulation, which are forecasted. Errors in the winds can greatly affect the estimate using this top-down approach (Valin et al., 2013; de Foy et al., 2014).

20   For the standard product, the effective NO_2 photochemical lifetime is 4.2 ± 1.7 hours, while in the regional product, the effective lifetime is 3.4 ± 1.4 hours. In the standard product, we derive the NO_x emissions rate to be 353 ± 146 kton/yr NO_2 equivalent, while in the regional product it is 484 ± 201 kton/yr NO_2 equivalent. Emission estimates using satellite products with coarse resolution air mass factors will yield top-down emission estimates that are lower than reality. In this case, the regional satellite product yields NO_x emission rates that are 37% higher; we would expect
25   similar results from other metropolitan regions. The top-down approach for the model simulation yielded a NO_x emission rate of 227 kton/yr, while the top-down approach using the satellite data yielded a 484 kton/yr NO_x emission rate: a 53% underestimate in the emissions inventory.

3.6. Model simulation with Double NO_x

To test whether a doubling in the NO_x emission rate is appropriate for the Seoul metropolitan area, we conduct a
30   simulation with NO_x emission increased by a factor of two. We analyzed the results for two days: May 17, 2016 and May 18, 2016. These two days had slow winds speeds and were indicative of days in which local emission sources had a dominating effect on the air quality. When comparing the model simulation to in situ observations from the UC-Berkeley NO_2 instrument aboard the DC-8 aircraft, we find that NO_2 concentrations are in good agreement with

11

Atmospheric
Chemistry
and Physics
Discussions

WRF-Chem in the boundary layer when spatially and temporally co-located in the immediate Seoul metropolitan area (Figure 9). This suggests that a doubling of NO_x in the inventory is appropriate.

Conclusions and Discussion

In this work, we use a high-resolution (4×4 km^2) WRF-Chem model simulation to re-calculate satellite NO_2 air mass factors over South Korea. We also apply a spatial averaging kernel to better account for the sub-pixel variability that cannot be observed by OMI. The regional OMI NO_2 retrieval yields increased tropospheric columns in city centers and near large industrial areas. In the area within 40 km of the Seoul city center, OMI NO_2 values are 1.37 larger in the regional product. Areas near large industrial sources have OMI NO_2 values that are >2 times larger. The increase in remotely sensed tropospheric vertical column contents in the Seoul metropolitan area is in better agreement with the Pandora NO_2 spectrometer measurements acquired during the KORUS-AQ field campaign.

Using the regional OMI NO_2 product with only the air mass factor correction applied, we derive the NO_x emissions rate from the Seoul metropolitan area to be 484 ± 201 kton/yr, while the standard NASA OMI NO_2 product gives an emissions rate of 353 ± 146 kton/yr. The WRF-Chem simulation yields a mid-afternoon NO_x emission rate of 227 ± 94 kton/yr. This suggests an underestimate in the bottom-up NO_x emissions from Seoul metropolitan area by 53%, when compared to the 484 kton/yr emissions rate from our top-down method. When comparing observed OMI NO_2 to the WRF-Chem model simulation, we find similar underestimates of NO_2 in the Seoul metropolitan area. Interestingly, when comparing NO_2 to aircraft observations, we find that the underestimate exists primarily in the Seoul metropolitan area, but not in more rural areas of the country. This suggests that perhaps the NO_x emission underestimate is primarily confined to the Seoul metropolitan area.

The effective photochemical lifetime derived in the Seoul plume is 4.2 ± 1.7 hours using the standard OMI NO_2 product and 3.4 ± 1.4 hours using the regional product. The regional product yields shorter NO_2 lifetimes, although it is not a statistically significant difference. It should be noted that the NO_2 photochemical lifetime derived here is a fundamentally different quantity than the NO_2 lifetime observed by in situ measurements (de Foy et al., 2014; Lu et al., 2015) or derived by model simulations (Lamsal et al., 2010). This is because the lifetime calculation is extremely sensitive to the accuracy of the wind direction. Inaccuracies in the wind fields introduce noise that shorten the tail of the fit. As a result, NO_2 photochemical lifetimes derived here are considered "effective" photochemical lifetimes and are universally shorter than the tropospheric column NO_2 lifetimes derived by model simulations (Lamsal et al., 2010). The effective photochemical lifetime is also different than a NO_2 lifetime derived by in situ measurements observing NO_2 at the surface or within the boundary layer: boundary layer where NO_2 is consumed faster yielding lifetimes that are shorter compared to the tropospheric column lifetimes (Nunnermacker et al., 2007).

We demonstrate that the temporalization of NO_x emissions in the bottom-up emission inventory is a large remaining uncertainty. The satellite-derived emission rates are instantaneous rates at the time of the OMI overpass (~13:45 local time). This is a different quantity than a bottom-up NO_x emission inventory which is often a daily averaged or monthly averaged emission rate. For this study, we only attempt to derive a mid-afternoon NO_x emission rate. Subsequently,

we make sure to compare this to the mid-afternoon NO $_x$ emission rate from WRF-chem. While bottom-up studies provide estimates of the diurnal variability of NO_x emissions, these are very difficult to confirm from top-down approaches. Due to a consistent mid-afternoon overpass time, OMI or TROPOMI cannot address this issue. Due to boundary layer dynamics, this is also very difficult to constrain from ground-based and aircraft measurements. In the

5   future, observations from a geostationary satellite instruments such as the Geostationary Environment Monitoring Spectrometer (GEMS) and Tropospheric Emissions: Monitoring Pollution (TEMPO), will be helpful in constraining the ratio of the mid-afternoon emissions rate to the 24-hour averaged emission rate.

Atmospheric
Chemistry
and Physics
Discussions

References

Allen, D. J., Pickering, K. E., Pinder, R. W., Henderson, B. H., Appel, K. W., and Prados, A.: Impact of lightning-NO on eastern United States photochemistry during the summer of 2006 as determined using the CMAQ model, Atmos. Chem. Phys., 12, 1737-1758, 2012.

5   Beirle, S., Boersma, K. F., Platt, U., Lawrence, M. G., and Wagner, T.: Megacity Emissions and Lifetimes of Nitrogen Oxides Probed from Space, Science, 333, 1737-1739, 2011.

Boersma, K. F., Jacob, D. J., Bucsela, E. J., Perring, A. E., Dirksen, R., Yantosca, R. M., Park, R. J., Wenig, M. O., Bertram, T. H., and Cohen, R. C.: Validation of OMI tropospheric NO_2 observations during INTEX-B and application to constrain NOx emissions over the eastern United States and Mexico, Atmos. Environ., 42, 4480-
10   4497, 2008.

Boersma, K. F., Eskes, H. J., Dirksen, R. J., Veefkind, J. P., Stammes, P., Huijnen, V., Kleipool, Q. L., Sneep, M., Claas, J., and Leitão, J.: An improved tropospheric NO2 column retrieval algorithm for the Ozone Monitoring Instrument, Atmos. Meas. Tech., 4, 1905, 2011.

Boersma, K. F., Vinken, G. C. M., and Tournadre, J.: Ships going slow in reducing their NOx emissions: changes in
15   2005–2012 ship exhaust inferred from satellite measurements over Europe, Environ. Res. Lett., 10, 074007,

Bucsela, E., Krotkov, N., Celarier, E., Lamsal, L., Swartz, W., Bhartia, P., Boersma, K., Veefkind, J., Gleason, J., and Pickering, K.: A new algorithm for retrieving vertical column NO2 from nadir-viewing satellite instruments: applications to OMI, Atmos. Meas. Tech, 6, 1361-1407, 2013.

Canty, T. P., Hembeck, L., Vinciguerra, T. P., Anderson, D. C., Goldberg, D. L., Carpenter, S. F., Allen, D. J.,
20   Loughner, C. P., Salawitch, R. J., and Dickerson, R. R.: Ozone and NOx chemistry in the eastern US: evaluation of CMAQ/CB05 with satellite (OMI) data, Atmos. Chem. Phys., 15, 10965-10982, 2015.

Chen, D., Zhou, B., Beirle, S., Chen, L. M., and Wagner, T.: Tropospheric NO_2 column densities deduced from zenith-sky DOAS measurements in Shanghai, China, and their application to satellite validation, Atmos. Chem. Phys., 9, 3641-3662, 2009.

25   Curier, R. L., Kranenburg, R., Segers, A. J. S., Timmermans, R. M. A., and Schaap, M.: Synergistic use of OMI NO_2 tropospheric columns and LOTOS–EUROS to evaluate the NOx emission trends across Europe, Remote Sensing of Environment, 149, 58-69, 2014.

Day, D. A., Wooldridge, P. J., Dillon, M. B., Thornton, J. A., and Cohen, R. C.: A thermal dissociation laser-induced fluorescence instrument for in situ detection of NO_2, peroxy nitrates, alkyl nitrates, and HNO_3, J. Geophys. Res.
30   Atmos., 107, ARTN 4046, 2002.

de Foy, B., Lu, Z., and Streets, D. G.: Impacts of control strategies, the Great Recession and weekday variations on NO_2 columns above North American cities, Atmos. Environ., 138, 74-86, 2016a.

de Foy, B., Lu, Z., and Streets, D. G.: Satellite NO_2 retrievals suggest China has exceeded its NOx reduction goals from the twelfth Five-Year Plan, Scientific Reports, 6, 2016b.

35   de Foy, B., Lu, Z., Streets, D. G., Lamsal, L. N., and Duncan, B. N.: Estimates of power plant NOx emissions and lifetimes from OMI NO_2 satellite retrievals, Atmos. Environ., 116, 1-11, 2015.

de Foy, B., Wilkins, J. L., Lu, Z., Streets, D. G., Duncan, B. N.: Model evaluation of methods for estimating surface emissions and chemical lifetimes from satellite data. Atmos. Environ. 98, 66-77, 2014.

Dobber, M., Kleipoo, Q., Dirksen, E., Levelt, P., Jaross, G., Taylor, S., Kelly, T., Flynn, L., Leppelmeier, G., and
40   Rozemeijer, N.: Validation of Ozone Monitoring Instrument level 1b data products, J. Geophys. Res. Atmos., 113, D15S06, 2008.

Ghude, S.D., Kulkarni, S.H., Jena, C., Pfist Duncan, B. N., Lamsal, L. N., Thompson, A. M., Yoshida, Y., Lu, Z., Streets, D. G., Hurwitz, M. M., and Pickering, K. E.: A space based, high resolution view of notable changes in urban NOx pollution around the world (2005–2014), J. Geophys. Res. Atmos., 121, 976-996, 2016.

45   Flynn, C. M., Pickering, K. E., Crawford, J. H., Lamsal, L., Krotkov, N., Herman, J., Weinheimer, A., Chen, G., Liu, X., and Szykman, J.: Relationship between column-density and surface mixing ratio: Statistical analysis of O_3 and NO_2 data from the July 2011 Maryland DISCOVER-AQ mission, Atmos. Environ., 92, 429-441, 2014.

Goldberg, D. L., Lamsal, L. N., Loughner, C. P., Swartz, W. H., Lu, Z., and Streets, D. G.: A high-resolution and observationally constrained OMI NO2 satellite retrieval, Atmos. Chem. Phys., 17, 11403-11421,
50   https://doi.org/10.5194/acp-17-11403-2017, 2017.

Goldberg, D. L., Vinciguerra, T. P., Anderson, D. C., Hembeck, L., Canty, T. P., Ehrman, S. H., Martins, D. K., Stauffer, R. M., Thompson, A. M., Salawitch, R. J., and Dickerson R. R.: CAMx ozone source attribution in the eastern United States using guidance from observations during DISCOVER-AQ Maryland, Geophys. Res. Lett., 43, https://dx.doi.org/10.1002/2015GL067332, 2016.

Grell, G., Peckham, S. E., Schmitz, R., McKeen, S. A., Frost, G., Skamarock, W. C., and Eder, B.: Fully coupled "online" chemistry within the WRF model, Atmospheric Environment, 39, 6957-6975, 10.1016/j.atmosenv.2005.04.027, 2005.

Han, K. M., Lee, S., Chang, L. S., and Song, C. H.: A comparison study between CMAQ-simulated and OMI-retrieved NO_2 columns over East Asia for evaluation of NOx emission fluxes of INTEX-B, CAPSS, and REAS inventories, Atmos. Chem. Phys., 15, 1913-1938, 2015.

Herman, J., Cede, A., Spinei, E., Mount, G., Tzortziou, M., and Abuhassan, N.: NO_2 column amounts from ground-based Pandora and MFDOAS spectrometers using the direct-sun DOAS technique: Intercomparisons and application to OMI validation, J. Geophys. Res., 114, D13307, 2009.

Heue, K.-P., Wagner, T., Broccardo, S. P., Walter, D., Piketh, S. J., Ross, K. E., Beirle, S., and Platt, U.: Direct observation of two dimensional trace gas distributions with an airborne Imaging DOAS instrument, Atmos. Chem. Phys., 8, 6707-6717, 2008.

Hilboll, A., Richter, A., and Burrows, J. P.: Long-term changes of tropospheric NO_2 over megacities derived from multiple satellite instruments, Atmos. Chem. Phys., 13, 4145-4169, 2013.

Hodzic, A., and Jimenez, J. L.: Modeling anthropogenically controlled secondary organic aerosols in a megacity: a simplified framework for global and climate models, Geosci. Model Dev., 4, 901-917, 10.5194/gmd-4-901-2011, 2011.

Hudman, R. C., Russell, A. R., Valin, L. C., and Cohen, R. C.: Interannual variability in soil nitric oxide emissions over the United States as viewed from space, Atmos. Chem. Phys., 10, 9943-9952, 2010.

Huijnen, V., Eskes, H. J., Poupkou, A., Elbern, H., Boersma, K. F., Foret, G., Sofiev, M., Valdebenito, A., Flemming, J., Stein, O., Gross, A., Robertson, L., D'Isidoro, M., Kioutsioukis, I., Friese, E., Amstrup, B., Bergstrom, R., Strunk, A., Vira, J., Zyryanov, D., Maurizi, A., Melas, D., Peuch, V.-H., and Zerefos, C.: Comparison of OMI NO_2 tropospheric columns with an ensemble of global and European regional air quality models, Atmos. Chem. Phys., 10, 3273-3296, doi:10.5194/acp-10-3273-2010, 2010.

Ialongo, I., Herman, J., Krotkov, N., Lamsal, L., Boersma, K. F., Hovila, J., and Tamminen, J.: Comparison of OMI NO_2 observations and their seasonal and weekly cycles with ground-based measurements in Helsinki, Atmos. Meas. Tech., 9, 5203, 2016.

Inness, A., Blechschmidt, A. M., Bouarar, I., Chabrillat, S., Crepulja, M., Engelen, R. J., Eskes, H., Flemming, J., Gaudel, A., Hendrick, F., Huijnen, V., Jones, L., Kapsomenakis, J., Katragkou, E., Keppens, A., Langerock, B., de Mazière, M., Melas, D., Parrington, M., Peuch, V. H., Razinger, M., Richter, A., Schultz, M. G., Suttie, M., Thouret, V., Vrekoussis, M., Wagner, A., and Zerefos, C.: Data assimilation of satellite retrieved ozone, carbon monoxide and nitrogen dioxide with ECMWF's Composition-IFS, Atmos. Chem. Phys. Discuss., 15, 4265-4331, 10.5194/acpd-15-4265-2015, 2015.

Kim, H. C., Lee, P., Judd, L., Pan, L., and Lefer, B.: OMI NO_2 column densities over North American urban cities: the effect of satellite footprint resolution, Geosci. Mod. Dev., 9, 1111-1123, 2016.

Kleipool, Q. L., Dobber, M. R., de Haan, J. F., and Levelt, P. F.: Earth surface reflectance climatology from 3 years of OMI data, J. Geophys. Res, Atmos,, 113, 2008.

Kowalewski, M. G., and Janz, S. J.: Remote sensing capabilities of the airborne compact atmospheric mapper, Proc. SPIE 7452, 74520Q, 2009.

Krotkov, N. A., McLinden, C. A., Li, C., Lamsal, L. N., Celarier, E. A., Marchenko, S. V., Swartz, W. H., Bucsela, E. J., Joiner, J., and Duncan, B. N.: Aura OMI observations of regional SO_2 and NO_2 pollution changes from 2005 to 2014, Atmos. Chem. Phys., 16, 4605-4629, 2016.

Krotkov, N. A., Lamsal, L. N., Celarier, E. A., Swartz, W. H., Marchenko, S. V., Bucsela, E. J., Chan, K. L., and Wenig, M. O.: The version 3 OMI NO_2 standard product, Atmos. Meas. Tech. Discuss., in review, 2017.

Kuhlmann, G., Lam, Y. F., Cheung, H. M., Hartl, A., Fung, J. C. H., Chan, P. W., and Wenig, W. O.: Development of a custom OMI NO_2 data product for evaluating biases in a regional chemistry transport model, Atmos. Chem. Phys., 15, 5627-5644, 2015.

Lamsal, L. N., Martin, R. V., van Donkelaar, A., Steinbacher, M., Celarier, E. A., Bucsela, E., Dunlea, E. J., and Pinto, J. P.: Ground-level nitrogen dioxide concentrations inferred from the satellite-borne Ozone Monitoring Instrument, J. Geophys. Res., 113, D16308, 2008.

Lamsal, L. N., Krotkov, N. A., Celarier, E. A., Swartz, W. H., Pickering, K. E., Bucsela, E. J., Gleason, J. F., Martin, R. V., Philip, S., and Irie, H.: Evaluation of OMI operational standard NO_2 column retrievals using in situ and surface-based NO_2 observations, Atmos. Chem. Phys., 14, 11587-11609, 2014.

Lamsal, L. N., Duncan, B. N., Yoshida, Y., Krotkov, N. A., Pickering, K. E., Streets, D. G., and Lu, Z.: US NO_2 trends (2005 - 2013): EPA Air Quality System (AQS) data versus improved observations from the Ozone Monitoring Instrument (OMI), Atmos. Environ., 110, 130-143, 2015.

Atmospheric
Chemistry
and Physics
Discussions
Open Access

Lamsal, L. N., Janz, S. J., Krotkov, N. A., Pickering, K. E., Spurr, R. J. D., Kowalewski, M. G., Loughner, C. P., Crawford, J. H., Swartz, W. H., and Herman, J. R.: High-resolution NO_2 observations from the Airborne Compact Atmospheric Mapper: Retrieval and validation, J. Geophys. Res. Atmos., 122, 1953-1970, 2017.

5   Laughner, J. L., Zare, A., and Cohen, R. C.: Effects of daily meteorology on the interpretation of space-based remote sensing of NO_2, Atmos. Chem. Phys., 16, 15247-15264, 2016.

Lee, H. J., and Koutrakis, P.: Daily ambient NO_2 concentration predictions using satellite ozone monitoring instrument NO_2 data and land use regression, Environ. Sci. & Tech., 48, 2305-2311, 2014.

Levelt, P. F., Van den Oord, G. H. J., Dobber, M. R., Malkki, A., Visser, H., de Vries, J., Stammes, P., Lundell, J. O. V., and Saari, H.: The Ozone Monitoring Instrument, IEEE Trans. Geosci. Rem. Sens., 44, 1093-1101, 2006.

10   Liaskos, C. E., Allen, D. J., and Pickering, K. E.: Sensitivity of tropical tropospheric composition to lightning NOx production as determined by replay simulations with GEOS-5, J. Geophys. Res. Atmos., 2015.

Lin, J. T., Liu, M. Y., Xin, J. Y., Boersma, K. F., Spurr, R., Martin, R., and Zhang, Q.: Influence of aerosols and surface reflectance on satellite NO_2 retrieval: seasonal and spatial characteristics and implications for NOx emission constraints, Atmos. Chem. Phys, 15, 11217-11241, 2015.

15   Lorente, A., Boersma, K. F., Yu, H., Dörner, S., Hilboll, A., Richter, A., Liu, M., Lamsal, L. N., Barkley, M., and De Smedt, I.: Structural uncertainty in air mass factor calculation for NO 2 and HCHO satellite retrievals, Atmos. Meas. Tech., 10, 759, 2017.

Lu, Z., and Streets, D. G.: Increase in NOx emissions from Indian thermal power plants during 1996–2010: unit-based inventories and multisatellite observations, Environ. Sci. & Tech., 46, 7463-7470, 2012.

20   Lu, Z., Streets, D. G., de Foy, B., Lamsal, L. N., Duncan, B. N., and Xing, J.: Emissions of nitrogen oxides from US urban areas: estimation from Ozone Monitoring Instrument retrievals for 2005–2014, Atmos. Chem. Phys., 15, 10367-10383, 2015.

Ma, J. Z., Beirle, S., Jin, J. L., Shaiganfar, R., Yan, P., and Wagner, T.: Tropospheric NO2 vertical column densities over Beijing: results of the first three years of ground-based MAX-DOAS measurements (2008–2011) and 25   satellite validation, Atmos. Chem. Phys., 13, 1547-1567, 2013.

Martin, R. V., Chance, K., Jacob, D. J., Kurosu, T. P., Spurr, R. J. D., Bucsela, E., Gleason, J. F., Palmer, P. I., Bey, I., and Fiore, A. M.: An improved retrieval of tropospheric nitrogen dioxide from GOME, J. Geophys. Res. Atmos., 107, 2002.

Martin, R. V., Jacob, D. J., Chance, K., Kurosu, T. P., Palmer, P. I., and Evans, M. J.: Global inventory of nitrogen 30   oxide emissions constrained by space-based observations of NO_2 columns, J. Geophys. Res. Atmos., 108, 2003.

McLinden, C. A., Fioletov, V., Krotkov, N. A., Li, C., Boersma, K. F., and Adams, C.: A Decade of Change in NO_2 and SO_2 over the Canadian Oil Sands As Seen from Space, Environ. Sci. & Tech., 50, 331-337, 2015.

Nault, B. A., Laughner, J. L., Wooldridge, P. J., Crounse, J. D., Dibb, J., Diskin, G., Peischl, J., Podolske, J. R., Pollack, I. B., Ryerson, T. B., Scheuer, E., Wennberg, P. O., and Cohen, R. C.: Lightning NOx Emissions: 35   Reconciling Measured and Modeled Estimates With Updated NOx Chemistry, Geophys. Res. Lett., 44, 9479– 9488, https://doi.org/10.1002/2017GL074436, 2017.

Palmer, P. I., Jacob, D. J., Chance, K. V., Martin, R. V., Spurr, R. J. D., Kurosu, T., Bey, I., Yantosca, R. M., Fiore, A., and Li, Q.: Air mass factor formulation for spectroscopic measurements from satellites: Application to formaldehyde retrievals from the Global Ozone Monitoring Experiment, J. Geophys. Res., 106, 14539-14550, 40   2001.

Pfister, G. G., Walters, S., Lamarque, J. F., Fast, J., Barth, M. C., Wong, J., Done, J., Holland, G., and Bruyère, C. L.: Projections of future summertime ozone over the U.S, Journal of Geophysical Research: Atmospheres, 119, 5559-5582, 10.1002/2013jd020932, 2014.

Pickering, K. E., Bucsela, E., D, Ring, A., Holzworth, R., and Krotkov, N.: Estimates of lightning NOx production 45   based on OMI NO_2 observations over the Gulf of Mexico, J. Geophys. Res. Atmos., 121, 8668-8691, 2016.

Platt, U.: Differential optical absorption spectroscopy (DOAS), Air monitoring by spectroscopic technique, 127, 27-84, 1994.

Pujadas, M., Núñez, L., and Lubrani, P.: Assessment of NO_2 satellite observations for en-route aircraft emissions detection, Remote Sensing of Environment, 115, 3298-3312, 2011.

50   Rasool, Q. Z., Zhang, R., Lash, B., and Cohan, D. S., Cooter, E. J., Bash, J. O., Lamsal, L. N.: Enhanced representation of soil NO emissions in the Community Multiscale Air Quality (CMAQ) model version 5.0. 2, Geosci. Mod. Dev., 9, 3177-3197, 2016.

Ridley, B. A., Dye, J. E., Walega, J. G., Zheng, J., Grahek, F. E., and Rison, W.: On the production of active nitrogen by thunderstorms over New Mexico, J. Geophys. Res. Atmos., 101, 20985-21005, 1996.

55   Russell, A. R., Valin, L. C., Bucsela, E. J., Wenig, M. O., and Cohen, R. C.: Space-based constraints on spatial and temporal patterns of NOx emissions in California, 2005-2008, Environ. Sci. Technol., 44, 3608-3615, 2010.

Russell, A. R., Perring, A. E., Valin, L. C., Bucsela, E. J., Browne, E. C., Wooldridge, P. J., and Cohen, R. C.: A high spatial resolution retrieval of NO_2 column densities from OMI: method and evaluation, Atmos. Chem. Phys., 11, 8543-8554, 2011.

5   Saide, P. E., Carmichael, G. R., Liu, Z., Schwartz, C. S., Lin, H. C., da Silva, A. M., and Hyer, E.: Aerosol optical depth assimilation for a size-resolved sectional model: impacts of observationally constrained, multi-wavelength and fine mode retrievals on regional scale forecasts, Atmos. Chem. Phys. Discuss., 13, 12213-12261, 10.5194/acpd-13-12213-2013, 2013.

Saide, P. E., Kim, J., Song, C. H., Choi, M., Cheng, Y., and Carmichael, G. R.: Assimilation of next generation geostationary aerosol optical depth retrievals to improve air quality simulations, Geophysical research letters, 41,
10   2014GL062089, 10.1002/2014gl062089, 2014.

Skamarock, W. C., Klemp, J. B., Dudhia, J., Gill, D. O., Barker, D. M., Duda, M. G., Huang, X.-Y., Wang, W., and Powers, J. G.: A description of the Advanced Research WRF version 3, NCAR Tech. Note NCAR/TN-475+ STR, 2008.

Souri, A. H., Choi, Y., Jeon, W., Li, X., Pan, S., Diao, L., and Westenbarger, D. A.: Constraining NOx emissions
15   using satellite NO_2 measurements during 2013 DISCOVER-AQ Texas campaign, Atmos. Environ., 131, 371-381, 2016.

Souri, A. H., Choi, Y., Jeon, W., Woo, J., Zhang, Q., and Kurokawa, J.: Remote sensing evidence of decadal changes in major tropospheric ozone precursors over East Asia J. Geophys. Res, Atmos., 2017.

Strahan, S. E., Duncan, B. N., and Hoor, P.: Observationally derived transport diagnostics for the lowermost
20   stratosphere and their application to the GMI chemistry and transport model, Atmos. Chem. Phys., 7, 2435-2445, 2007.

Streets, D. G., Canty, T., Carmichael, G. R., de Foy, B., Dickerson, R. R., Duncan, B. N., Edwards, D. P., Haynes, J. A., Henze, D. K., Houyoux, M. R., Jacob, D. J., Krotkov, N. A., Lamsal, L. N., Liu, Y., Lu, Z., Martin, R. V., Pfister, G. G., Pinder R. W., Salawitch, R. J., Wecht, K. J.: Emissions estimation from satellite retrievals: A
25   review of current capability, Atmos. Environ., 77, 1011-1042, 2013.

Strode, S. A., Rodriguez, J. M., Logan, J. A., Cooper, O. R., Witte, J. C., Lamsal, L. N., Damon, M., Van Aartsen, B., Steenrod, S. D., and Strahan, S. E.: Trends and variability in surface ozone over the United States, J. Geophys. Res. Atmos., 120, 9020-9042, 2015.

Thornton, J. A., Wooldridge, P. J., and Cohen R. C.: Atmospheric NO_2: In situ laser-induced fluorescence detection
30   at parts per trillion mixing ratios, Analytical Chemistry, 72, 528-539, 2000.

Valin, L. C., Russell, A. R., and Cohen, R. C.: Variations of OH radicals in an urban plume inferred from NO_2 column measurements. Geophys. Res. Lett., 40, 1856-1860, 2013.

Val Martin, M., Honrath, R. E., Owen, R. C., Pfister, G., Fialho, P., and Barata, F.: Significant enhancements of nitrogen oxides, black carbon, and ozone in the North Atlantic lower free troposphere resulting from North
35   American boreal wildfires, J. Geophys. Res. Atmos., 111, 2006.

van der A, R. J., Mijling, B., Ding, J., Koukouli, M. E., Liu, F., Li, Q., Mao, H., Theys, N.: Cleaning up the air: effectiveness of air quality policy for SO_2 and NO_x emissions in China, Atmos. Chem. Phys., 17, 1775–1789, 2017.

van Donkelaar, A., Martin, R. V., Leaitch, R. W., Macdonald, A. M., Walker, T. W., Streets, D. G., Zhang, Q., Dunlea,
40   E. J., Jimenez, J. L., and Dibb, J. E.: Analysis of aircraft and satellite measurements from the Intercontinental Chemical Transport Experiment (INTEX-B) to quantify long-range transport of East Asian sulfur to Canada, Atmos. Chem. Phys., 8, 2999-3014, 2008.

van Vuuren, D. P., Bouwman, L. F., Smith, S. J., and Dentener, F.: Global projections for anthropogenic reactive nitrogen emissions to the atmosphere: an assessment of scenarios in the scientific literature, Current Opinion in
45   Environmental Sustainability, 3, 359-369, 2011.

Vandaele, A. C., Hermans, C., Simon, P. C., Carleer, M., Colin, R., Fally, S., Merienne, M.-F., Jenouvrier, A., and Coquart, B.: Measurements of the NO_2 absorption cross-section from 42 000 cm− 1 to 10 000 cm− 1 (238–1000 nm) at 220 K and 294 K, Journal of Quantitative Spectroscopy and Radiative Transfer, 59, 171-184, 1998.

Veefkind, J. P., Aben, I., McMullan, K., Förster, H., De Vries, J., Otter, G., Claas, J., Eskes, H. J., De Haan, J. F., and
50   Kleipool, Q.: TROPOMI on the ESA Sentinel-5 Precursor: A GMES mission for global observations of the atmospheric composition for climate, air quality and ozone layer applications, Remote Sensing of Environment, 120, 70-83, 2012.

Verstraeten, W. W., Neu, J. L., Williams, J. E., Bowman, K. W., Worden, J. R., and Boersma, K. F.: Rapid increases in tropospheric ozone production and export from China, Nat. Geosci., 8, 690, 2015.

55   Vinken, G. C. M., Boersma, K. F., Maasakkers, J. D., Adon, M., and Martin, R. V.: Worldwide biogenic soil NOx emissions inferred from OMI NO_2 observations, Atmos. Chem. Phys., 14, 10363-10381, 2014a.

Atmospheric
Chemistry
and Physics
Discussions

Vinken, G. C. M., Boersma, K. F., van Donkelaar, A., and Zhang, L.: Constraints on ship NOx emissions in Europe using GEOS-Chem and OMI satellite NO2 observations, Atmos. Chem. Phys., 14, 1353-1369, 2014b.

Young, M. T., Bechle, M. J., and Sampson, P. D., Szpiro, A. A., Marshall, J. D., Sheppard, L., and Kaufman, J. D.: Satellite-Based NO_2 and Model Validation in a National Prediction Model Based on Universal Kriging and Land-Use Regression, Environ. Sci. & Tech., 50, 3686-3694, 2016.

Zaveri, R. A., Easter, R. C., Fast, J. D., and Peters, L. K.: Model for simulating aerosol interactions and chemistry (MOSAIC), J. Geophys. Res, 113, D13204, 2008.

Zhang, L., Jacob, D. J., Boersma, K. F., Jaffe, D. A., Olson, J. R., Bowman, K. W., Worden, J. R., Thompson, A. M., Avery, M. A., Cohen, R. C., Dibb, J. E., Flock, F. M., Fuelberg, H. E., Huey, L. G., McMillan, W. W., Singh, H. B., and Weinheimer, A. J.: Transpacific transport of ozone pollution and the effect of recent Asian emission increases on air quality in North America: an integrated analysis using satellite, aircraft, ozonesonde, and surface observations, Atmos. Chem. Phys., 8, 6117-6136, 2008.

Zoogman, P., Liu, X., Suleiman, R. M., Pennington, W. F., Flittner, D. E., Al-Saadi, J. A., Hilton, B. B., Nicks, D. K., Newchurch, M. J., and Carr, J. L.: Tropospheric emissions: monitoring of pollution (TEMPO), Journal of Quantitative Spectroscopy and Radiative Transfer, 186, 17-39, 2017.
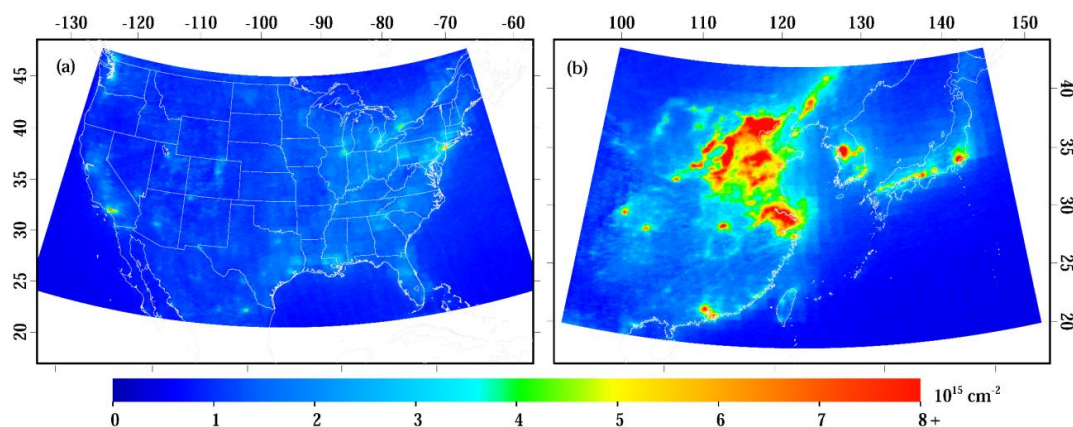
Atmospheric
Chemistry
and Physics
Discussions

Figure 1. Warm season averaged (May – Sept) NO₂ tropospheric column content using the standard OMI NO₂ product for years of 2015 – 2017 in (a) the United States and (b) East Asia.
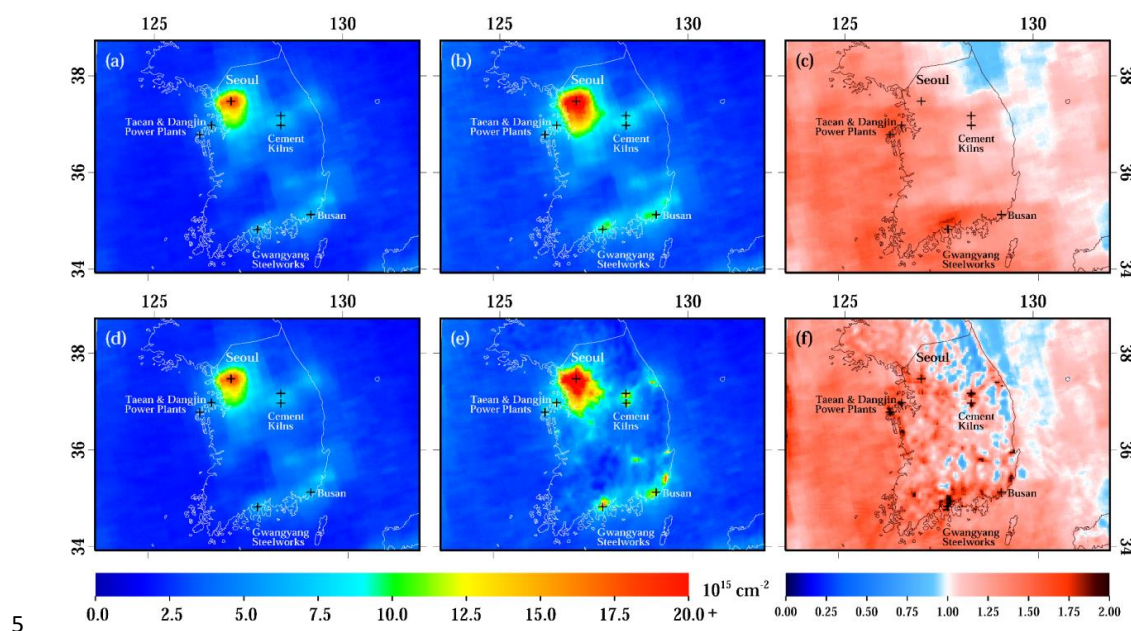

Figure 2. (a) OMI-Standard NO₂ product averaged over a 9-month period, Apr – Jun 2015 – 2017, (b) the OMI-Regional NO₂ product with only the air mass factor adjustment averaged over the same timeframe, and (c) the ratio between the two products. (d) Same as the top left plot, (e) the OMI-Regional NO₂ product with the air mass factor adjustment and spatial kernel averaged over the same timeframe, and (f) the ratio between the two products.

Atmospheric
Chemistry
and Physics
Discussions

Figure 3. (a) The OMI-Regional NO$_2$ product with the air mass factor adjustment and spatial kernel averaged during the month of May 2016, (b) the WRF-Chem model simulation showing only days with valid OMI measurements, and (c) the ratio between the two products. On average, there are only 9 valid OMI pixels per month observed at any given location on the Korean peninsula during May 2016.
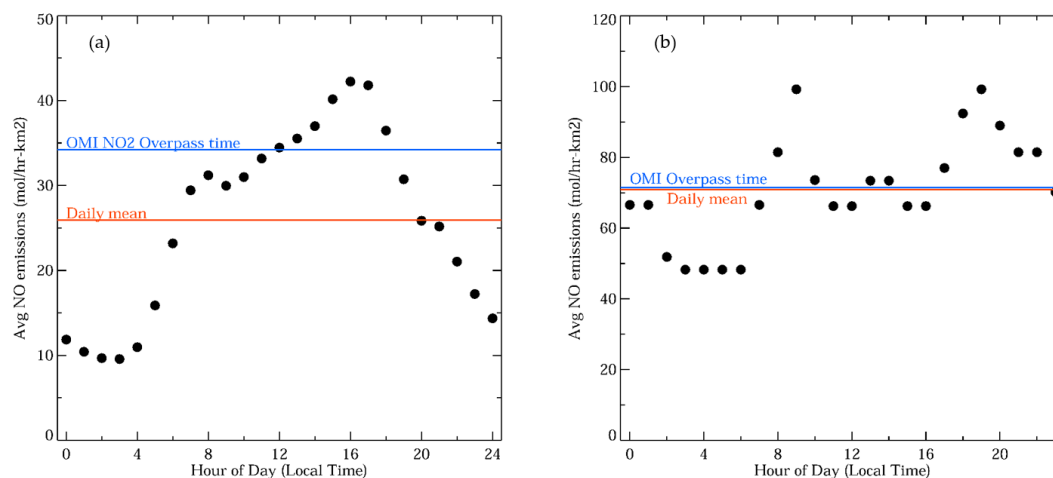

Figure 4. The diurnal profile of NO$_x$ emission rates processed from the bottom-up inventory. (a) The diurnal profile of NO$_x$ emission rates during a weekday in the eastern USA during July 2011 using SMOKE as the emissions pre-processor (Goldberg et al., 2016). (b) The diurnal profile of emission rates during a weekday in Korea during May 2016 using EPRES as the emissions pre-processor. Emission profiles in the right panel were used in the WRF-Chem simulation.
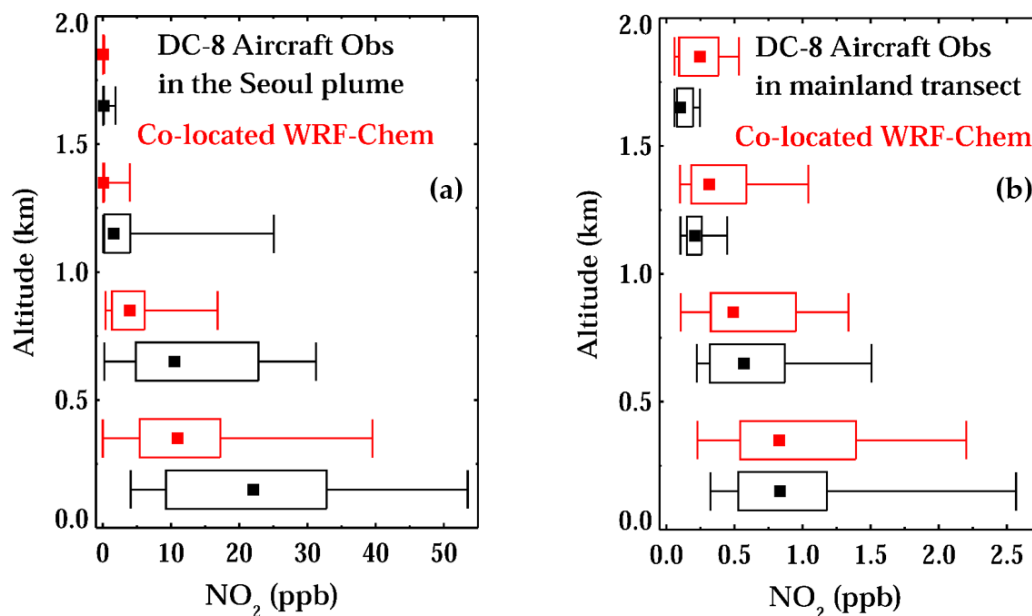
Figure 5. Measurements from the DC-8 aircraft binned by altitude in black. Co-located WRF-Chem within the same altitude bin as the aircraft observations are plotted above in red. Square dots represent the median values. (a) Comparison in the Seoul plume, and (b) Comparison along in the "mainland transect" – flights in the more rural areas of the Korean peninsula.
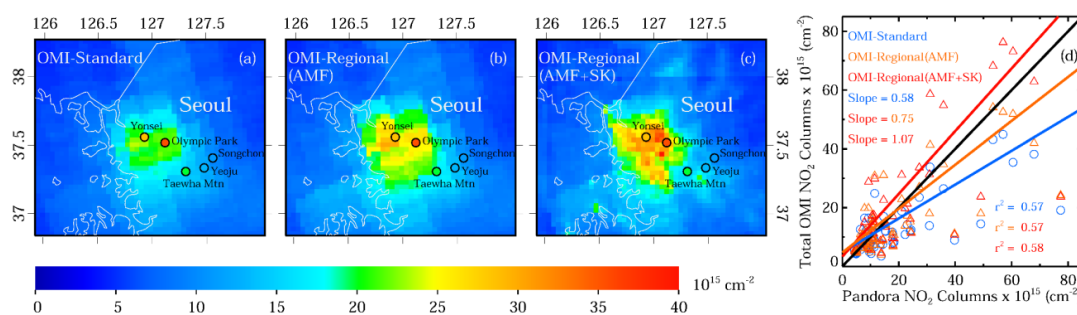

Figure 6. (a) Total column contents from the OMI-Standard NO$_2$ product for May 2016, (b) same quantities from the OMI-Regional product with only the air mass factor adjustment (AMF) during the same timeframe, (center right) same quantities from the OMI-Regional product with the air mass factor adjustment and spatial kernel (AMF+SK) during the same timeframe, and (c) a comparison between observed total column contents from OMI NO$_2$ and Pandora NO$_2$ during May 2016. An average of Pandora 2-hour means co-located to valid daily OMI overpasses are overlaid in the spatial plots.
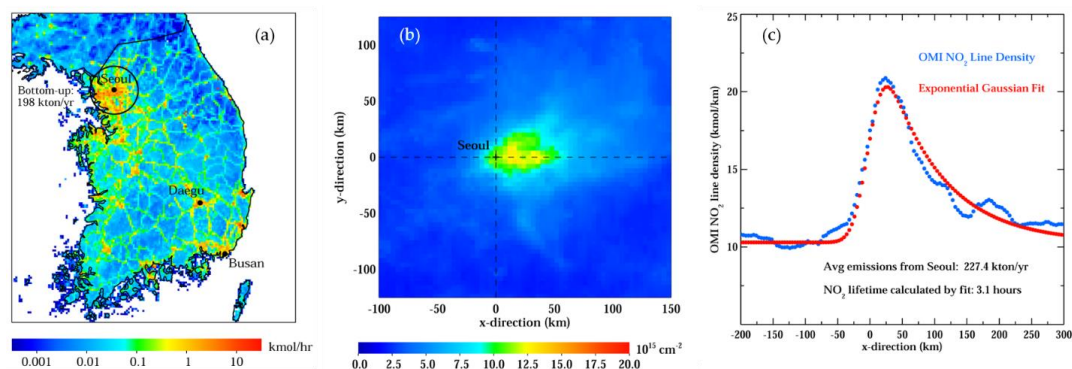
Atmospheric
Chemistry
and Physics
Discussions

Figure 7. (a) Bottom-up NO$_x$ emissions inventory compiled for the KORUS-AQ field campaign, (b) the oversampled NO$_2$ plume rotated based on wind direction for Seoul, Korea from WRF-Chem (4 × 4 km²) for May 2016, and (c) NO$_2$ line densities integrating over the 240 km across plume width (-120 km to 120 km along the y-axis) and the corresponding EMG fit. NO$_x$ emission estimates are shown in units of kton/yr NO$_2$ equivalent and represent the mid-afternoon emissions rate.
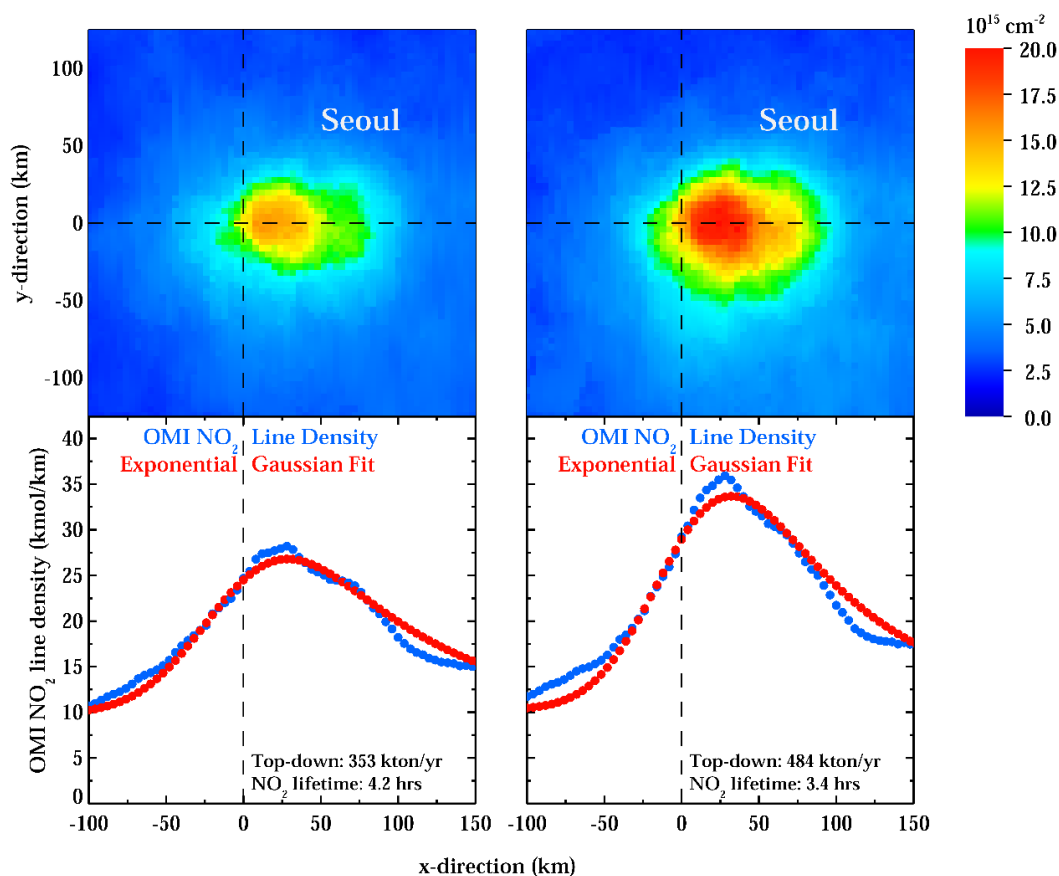
Figure 8. Top panels represent the oversampled (4×4 km^2) OMI NO$_2$ plume from Seoul rotated based on wind direction over a 9-month period, Apr – Jun 2015 – 2017, centered on May 2016. Bottom panels represent the OMI NO$_2$ line densities integrating over the 240 km across plume width (-120 km to 120 km along the y-axis of the top panels) and the corresponding EMG fit. Left panels are from the OMI-Standard NO$_2$ product and right panels are from the OMI-Regional NO$_2$ product. NO$_x$ emission estimates are shown in units of kton/yr NO$_2$ equivalent and represent the mid-afternoon emissions rate.
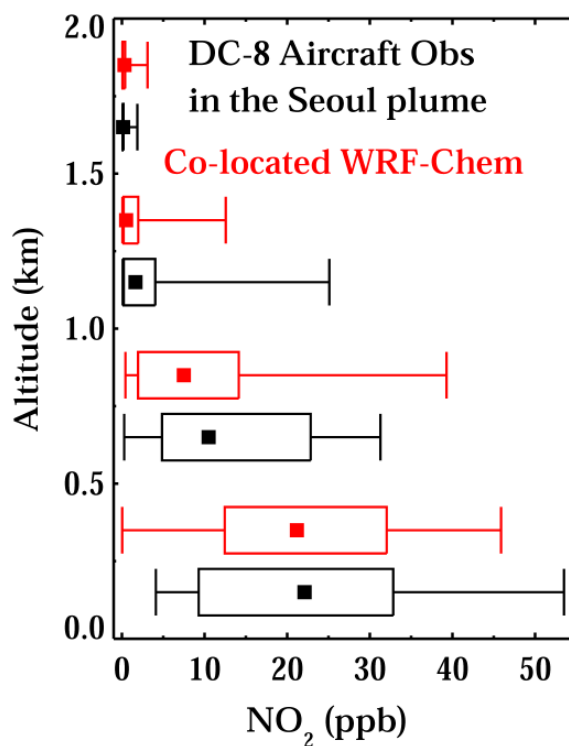
Figure 9. Comparison in the Seoul plume for May 17, 2016 and May 18, 2016 between aircraft measurements and a
$2 \times NO_x$ WRF-Chem simulation. DC-8 Aircraft measurements are binned by altitude in black. Co-located WRF-Chem
within the same altitude bin as the aircraft observations are plotted above in red. Square dots represent the median
values.